Available online at www.sciencedirect.com

SciVerse ScienceDirect

Journal of the European Ceramic Society 32 (2012) 1613–1624

www.elsevier.com/locate/jeurceramsoc

Thermal degradation of microporous Sm_2O_3–MgO nanocomposites at isothermal conditions and surface chemical properties

Thorsten Enz [a,*], Ralf Theissmann [b], Horst Hahn [a,c]

[a] *Joint Research Laboratory Nanomaterials, Technische Universität Darmstadt and Karlsruhe Institute of Technology, Petersenstrasse 23, 64287 Darmstadt, Germany*

[b] *Faculty of Engineering and Center for Nanointegration Duisburg-Essen (CeNIDE), University of Duisburg-Essen, Bismarckstrasse 81, 47057 Duisburg, Germany*

[c] *Institute of Nanotechnology, Karlsruhe Institute of Technology, Postfach 3640, 76021 Karlsruhe, Germany*

Received 7 July 2011; received in revised form 4 January 2012; accepted 8 January 2012
Available online 30 January 2012

Abstract

The evolution of microstructural, morphological and surface chemical properties of Sm_2O_3–MgO nanocomposites are determined during and after isothermal heat treatments in the range of 500–1000 °C. The samples are investigated using (high temperature) X-ray diffraction, energy-filtered transmission electron microscopy including electron energy loss spectroscopy, nitrogen adsorption, and temperature programmed desorption of CO_2. With small amounts of MgO the initial micropore fractions are low and mainly coarsening of Sm_2O_3 is observed. Large amounts of MgO result in high initial micropore fractions giving rise to enhanced densification. The different thermal degradation behaviors are explained by means of the respective characteristic diffusion distances which are determined by the volume phase fractions. The surface chemical properties of Sm_2O_3 and MgO remain qualitatively unchanged, however, the specific CO_2 chemisorption capacities are increased through the nanocomposite formation.

Keywords: Grain size; Interfaces; Nanocomposites; Porosity; Thermal degradation

1. Introduction

Nanoparticulate materials are in general characterized by spatial dimensions smaller than 100 nm and – since the ratio of surface area to volume is inversely proportional to the particle diameter – large amounts of specific surface area. This makes them ideal candidates for all applications where gaseous or liquid media shall interact with active surface sites.[1,2] Consequently, nanoparticulate materials quickly gained importance for large scale industrial applications in heterogeneous catalysis.[3] They are very often used as active or passive supports but may also serve as the catalyst. It is noted that in addition to just the increase in number density of active surface sites different types of nanostructure effects may further enhance the catalytic activity and selectivity.[4]

A field of growing importance in chemical and life science industry is the solid acid–base catalysis using single- or multicomponent metal oxides.[5] However, a serious issue of solid base catalysts is their high affinity towards oxygen, water, and especially carbon dioxide. This necessitates high pretreatment temperatures in the order of 1000 K for cleaning the surface and hence achieving the maximum of catalytic performance.[6] Furthermore, several chemical reactions also require high working temperatures. For example many of the catalysts tested for the oxidative coupling of methane (OCM) perform best at temperatures of 700–800 °C.[7] Unfortunately, high application temperatures are in conflict with the metastable nature of nanostructured materials. Thermally activated atomic mass transport reduces the Gibbs energy of the system by minimizing the area and curvature of particle surfaces and interfaces. Thermal degradation of catalysts is characterized by a loss of active or carrier surface area as well as phase transformation and grain growth of the active phase.[8] Thus, the ultimate ambition is not only to generate a maximum number density of active sites but also to stabilize this state to ensure a reasonable catalyst lifetime.[9]

* Corresponding author. Current address: Institut für Materialphysik im Weltraum, Deutsches Zentrum für Luft- und Raumfahrt (DLR), 51170 Köln, Germany.
E-mail address: thorsten.enz@dlr.de (T. Enz).

0955-2219/$ – see front matter © 2012 Elsevier Ltd. All rights reserved.
doi:10.1016/j.jeurceramsoc.2012.01.004

Rare earth oxides and alkaline earth oxides are well recognized groups of solid base catalysts.[10] Sm_2O_3 gained particular importance in heterogeneous catalysis after the work by Keller and Bhasin[11] encouraged the search for suitable catalysts for the OCM reaction (see e.g. [12–15]). From a whole series of metal oxides Sm_2O_3 showed the highest catalytic activity and selectivity[16] and was thus the subject of many investigations. In principle, MgO is also suited to activate the very strong C–H bonds of methane.[17] One of the most effective catalysts for the OCM reaction is produced by doping of MgO with lithium.[18,19] Furthermore, the properties of the system Sm_2O_3–MgO were investigated with respect to the OCM reaction, e.g. the activation mechanisms of methane and oxygen.[20,21] By impregnation of MgO with 5 wt% and 10 wt% Sm_2O_3 a significant increase in specific surface area compared to pure MgO was achieved after calcination at 700 °C.[22] However, no improvement of catalytic activity was observed. In contrast, Sm-promoted MgO produced from the corresponding acetates showed both higher catalytic activity and selectivity.[23]

Recently, we reported on the formation of Sm_2O_3–MgO nanocomposites.[24] Eight samples with different ratios of Sm_2O_3 to MgO were synthesized. Sample names are based on composition, such that e.g. $Sm_{45}Mg_{55}$ denotes a nanocomposite of 55 mol% Sm_2O_3 and 45 mol% MgO. Aqueous precursors were prepared from the corresponding nitrates and citric acid was added as a chelating agent. The liquid precursors were converted into powders using a spray pyrolysis setup operated at low temperature. The powders comprise micrometer sized hollow spheres with shells of less than 100 nm thickness. As a result of the low synthesis temperature the as prepared samples consist of amorphous metal carboxylate networks. Continuous heating rate experiments demonstrated that the grain growth of Sm_2O_3 can be slowed down by adding the immiscible MgO. The extensive microporosity common to all samples was supposed to have serious impact on the grain growth behavior. Here, we first investigate the grain growth behavior of these samples at isothermal conditions on long timescales. The evolution of grain size versus time is assessed by high temperature X-ray diffraction (HTXRD). After cool down to room temperature the HTXRD samples are characterized in detail by means of X-ray diffraction (XRD) and energy-filtered transmission electron microscopy (EFTEM) including electron energy loss spectroscopy (EELS). Furthermore, various batches of heat-treated nanocomposites are prepared from the starting materials for the measurement of nitrogen adsorption and temperature programmed desorption of CO_2 (CO_2–TPD). The results allow for the explanation of different thermal degradation behaviors depending on sample composition and temperature level.

2. Experimental procedure

The HTXRD measurements were performed with a Bruker AXS D8 Advance diffractometer (Bruker AXS, Karlsruhe, Germany) in θ–θ geometry. The samples were placed inside a high temperature chamber (Anton Paar HTK 1200N, Graz, Austria) on a corundum sample holder to provide a controllable sample environment. X-rays emitted by a copper tube were used to illuminate a constant sample length of 12 mm by means of a variable slit assembly. Primary and secondary Soller slits with 2.5° angle of acceptance were utilized to reduce the axial divergence. Cu K_α radiation was selected by placing a Ni-filter in front of the position sensitive detector (Bruker AXS VÅNTEC, Karlsruhe, Germany). In order to achieve high temporal resolution, sections of $2\theta = 10°$ were recorded simultaneously with fixed incident and diffracted beam angles of equal value. The acquisition time for each pattern was 1 min with an angular resolution of 0.022°. All measurements were conducted in static air atmosphere. For each sample separate runs were performed at 500 °C, 600 °C, 700 °C, 800 °C, 900 °C, and 1000 °C. Temperatures were ramped to the target values with 30 K/min which was the maximum rate possible with this equipment. Measurements were started as soon as isothermal conditions were established and stopped after a total duration of 12 h.

The XRD measurements were conducted in immediate succession to the HTXRD measurements using the same experimental setup. After cool down to room temperature $\theta - 2\theta$-scans were performed in order to obtain full XRD patterns.

Subsequently, some of the HTXRD samples were subjected to detailed EFTEM analyses. For that purpose a JEOL JEM-3010 microscope (JEOL Ltd., Tokyo, Japan) equipped with a Gatan Imaging Filter (GIF, Gatan, Inc., Pleasanton, CA) was used. An LaB_6 cathode operated at 300 kV served as the electron source. A small amount of sample was ultrasonically dispersed in methanol for a few minutes and one drop of this dispersion was deposited on a perforated carbon foil. Unfiltered bright field images were taken at low resolution using an analog camera. For obtaining high resolution bright field images only elastically scattered electrons were detected on a slow-scan CCD camera. The spatial distribution of samarium and magnesium was determined by means of EELS. Two pre-edge images and one post-edge image were captured at the samarium N-edge and the magnesium L-edge in order to compute element distribution maps.

For the nitrogen adsorption measurements the starting materials were weighed into measurement cells made of quartz glass. The loaded measurement cells were placed into a tubular furnace and repeatedly exposed to temperatures of 200 °C, 300 °C, 400 °C, 500 °C, 600 °C, 700 °C, 800 °C, 900 °C, and 1000 °C in static air atmosphere for 2 h each. After each heat treatment nitrogen adsorption isotherms were recorded with a Quantachrome Autosorb-3B system (Quantachrome, Boynton Beach, FL). Prior to the measurements samples were degassed at 200 °C in vacuum for at least 12 h.

The measurements of CO_2–TPD were performed using a Thermo Electron TPD/R/O 1100 instrument (Thermo Electron, Rodano, Italy). The starting materials were first heat-treated in a tubular furnace for 12 h at 800 °C in static air atmosphere and then weighed into flow-through cells made of quartz glass. After attaching the flow-through cells to the instrument the samples were heated in a stream of 20 sccm[1] 5.17 % O_2 in He with a rate of 10 K/min from room temperature to 800 °C. After 2 h they

[1] Standard cubic centimeter per minute.

were cooled back to room temperature in a stream of 20 sccm He. Immediately after this pretreatment the conditioned samples were exposed to 10 pulses of CO_2. Care was taken to ensure that the last pulses generated detector signals of identical magnitude, i.e. that no more CO_2 was adsorbed. Finally, using a carrier gas stream of 20 sccm He the CO_2–TPD measurements were performed by heating the samples to 800 °C with a rate of 10 K/min.

2.1. Data evaluation

The evaluation of (HT)XRD measurements was performed with the commercial software TOPAS version 3.0 (Bruker AXS, Karlsruhe, Germany). Only a simplified single peak analysis was applied to the HTXRD data because of the small snapshots recorded for the sake of temporal resolution. Individual peaks were fitted by means of the pseudo-Voigt function.[25] A single full width at half maximum (FWHM) was used for both the Lorentzian and Gaussian contributions and a 1st order polynom was taken into account to model a linear background. Hence, a total number of 6 parameters was sufficient to describe one peak without the need of any constraints or restraints. In detail, a mixing parameter for weighting the Lorentzian and Gaussian contributions, FWHM, peak position, intensity, and two background parameters were applied. From these results the integral breadth β_Q was calculated in terms of the scattering vector Q. Neglecting other sources of peak broadening, the inverse of β_Q can be used as a measure for grain size. The analysis of cubic Sm_2O_3 was carried out using the {2 2 2} peak which is of highest intensity. For pure MgO the second strongest {2 2 0} peak was chosen because of peak overlapping with the corundum sample holder. The analysis of MgO in presence of Sm_2O_3 was not feasible for the same reasons discussed previously.[24] The issues are weak intensities due to small structure factors and peak overlapping with Sm_2O_3 in conjunction with a rather low signal to noise ratio of the position sensitive detector. For all samples only peaks measured during the first 4 h and the last 2 h were evaluated. By this means the very dynamic beginning of grain growth as well as the approach of steady state conditions could be assessed without the need to analyze all data.

For the evaluation of full XRD patterns the fundamental parameters approach [26] was used. Instrument parameters were determined beforehand by doing a Rietveld refinement of the XRD pattern of a reference material LaB_6 (SRM 660a, National Institute of Standards & Technology, Gaithersburg, ML). At first, Williamson–Hall plots[27] were generated in order to identify the origin of sample induced peak broadening. Lorentz functions were independently fitted to single peaks in order to obtain β_Q which is a linear function of Q:

$$\beta_Q = Kd^{-1} + 2\epsilon Q \quad (1)$$

In Eq. (1) K is the Scherrer constant, d is the grain size, and ϵ is the upper limit of microstrain according to Stokes and Wilson.[28] Based on the semi-quantitative results a consistent approach to doing Rietveld refinements could be established. This did not primarily aim at achieving the best fit of individual XRD patterns but at obtaining the best comparability among different samples. Crystal structure data were taken from the Inorganic Crystal Structure Database (ICSD). In particular the structures of cubic Sm_2O_3 (space group *Ia*-3, ICSD# 40475), monoclinic Sm_2O_3 (space group *C*12/*m*1, ICSD# 202903), and cubic MgO (space group *Fm*-3*m*, ICSD# 52026) were considered.

Element distribution maps were generated from EFTEM images by means of the three windows method. For each pixel the absorption intensities of the samarium N-edge and the magnesium L-edge were calculated. A power law was applied to the pre-edge images to determine the background intensity being subtracted from the post-edge image. In order to reduce the noise the background intensity was smoothed by averaging five pixels at a time.

From nitrogen adsorption isotherms $\alpha_{0.4}$-plots were generated to track the development of specific surface area and porosity. The analyses were done following the procedure described in[24] using the same standard isotherms obtained from reference materials.

The CO_2–TPD curves were deconvoluted into individual desorption signals by means of an empirical fitting routine. At first, a baseline correction was performed by subtracting a 1st order polynom. The corrected data were fitted with the fewest possible number of independent Gaussian functions. A previously determined calibration factor was used to convert the area of the Gaussian functions into the corresponding amount of CO_2.

3. Results

3.1. High temperature X-ray diffraction

A first overview of the magnitude of grain growth is provided by a comparison of β_Q^{-1} values at the beginning (t= 0 min) and the end (t = 780 min) of the isothermal dwell time (Fig. 1). For both instants of time a distinct increase of β_Q^{-1} with temperature is observed for Sm_2O_3 as well as MgO. However, at t = 0 min the influence of MgO on the grain growth of Sm_2O_3 is not yet significant. Only at the end of the dwell time the grain growth inhibiting effect of MgO has fully developed.

In Fig. 2 grain growth curves of samples with three different compositions measured at the same temperature and of one sample measured at three different temperatures are exemplarily displayed. At 700 °C the initial rate and the total extent of grain growth are clearly higher for pure Sm_2O_3 than for pure MgO. At the same temperature grain growth of Sm_2O_3 in sample $Sm_{25}Mg_{75}$ is considerably slower and less pronounced. A change in temperature does not only affect the initial rate but also the duration of grain growth, i.e. the time needed to reach the steady state. At 900 °C Sm_2O_3 grows faster and longer compared to 700 °C. In contrast, at 500 °C grain growth is not observed at all.

3.2. X-ray diffraction

Williamson–Hall plots were generated for all samples containing Sm_2O_3 and being heat-treated at 500–800 °C. Samples treated at higher temperatures could not reliably be analyzed

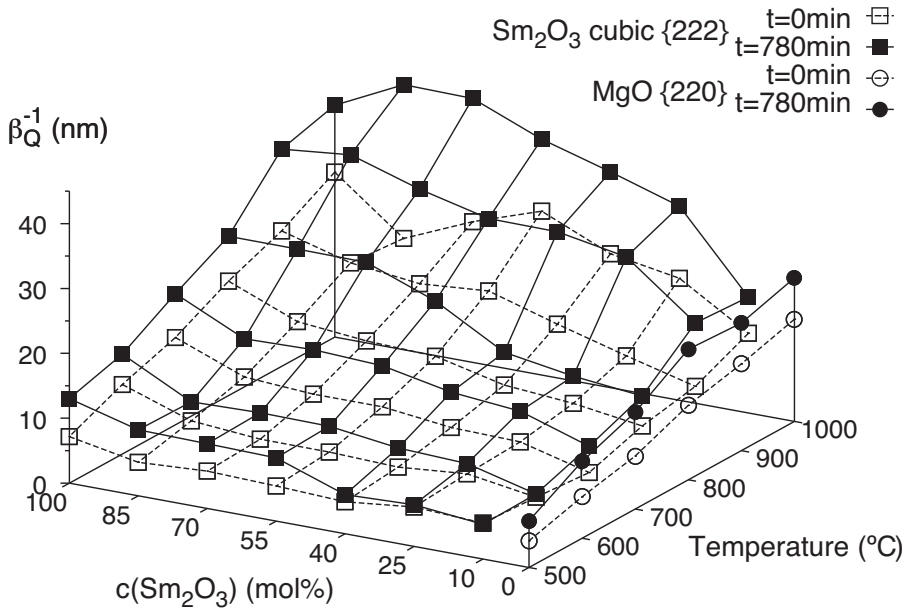

Fig. 1. Inverse of the integral breadth β_Q^{-1} determined from HTXRD at isothermal conditions at instants of $t = 0$ min and $t = 780$ min.

because the phase transformation from cubic to monoclinic Sm_2O_3 affected the accuracy of single peak fits. The six strongest peaks of cubic Sm_2O_3 were analyzed which sum up to more than 80 % of the total intensity and cover a sufficiently wide angular range. The only exception is sample $Sm_{10}Mg_{90}$ heat-treated at 500 °C where the two peaks at highest scattering angles and of lowest intensity are absent. A typical set of Williamson–Hall plots according to Eq. (1) is depicted in Fig. 3a. With rising temperature both the *y*-axis intercept and the slope show the tendency to decrease. This means that growth and relaxation processes based on thermally activated diffusion take place which lead to an increase in grain size and a decrease in microstrain. The effect of MgO is opposed to the effect of temperature. The more MgO the lower the grain size of Sm_2O_3 but the higher the initial microstrain.

Reliable quantitative results can hardly be extracted from the Williamson–Hall plots because especially at low temperatures and with large amounts of MgO the quality of fit suffers from scattered data. However, it can be stated that finite grain size is the predominant reason for sample induced peak broadening while a perceptible influence of microstrain is limited to low temperatures and large amounts of MgO.

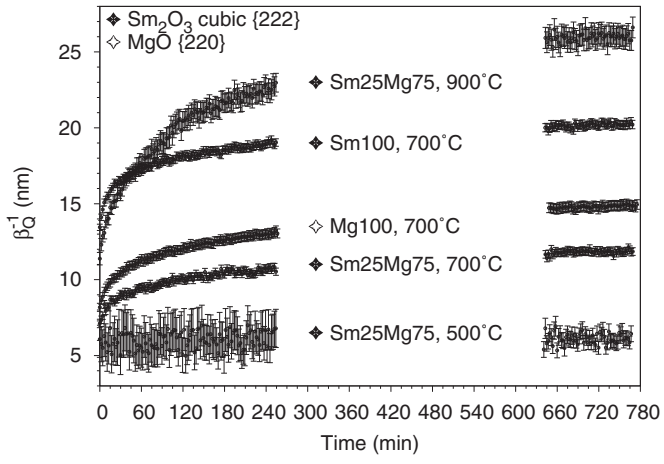

Fig. 2. Grain growth curves of samples Sm_{100}, $Sm_{25}Mg_{75}$, and Mg_{100} measured in static air atmosphere at the temperatures indicated.

This conclusion was the baseline for conducting Rietveld refinements of complete XRD patterns. The background was modeled by a 4th order polynom and the zero shift of XRD patterns was adapted by a variable sample height. Occasionally appearing peaks originating from the sample holder were masked by simultaneously fitting individual Lorentzian functions. A scaling factor was applied to each crystallographic phase. Lattice parameters and if applicable angles were refined while site occupancies were adopted unchanged from the database. Peak profiles were modeled step by step using the Double–Voigt approach.[29] At first, only a Lorentzian function was used to describe peak broadening due to finite grain size. A Gaussian function was added only if the error of integral breadth was not higher than the value itself. Otherwise, the excessive usage of fit parameters would have yielded arbitrary results having no physical significance.

Subsequently, an attempt was made to also take microstrain into account using a second set of Lorentzian and Gaussian functions. It turned out that the additional degrees of freedom do not significantly improve the quality of the refinement but yield large errors of both grain size and microstrain. The least squares method applied to fit the data puts emphasis on peaks with high intensity in order to minimize the sum of squared differences. In effect, peaks measured at high scattering angles being essential for identifying microstrain play only a minor role because of their low intensity. In other words, the influence of microstrain is not high enough to be clearly distinguished from finite grain size and thus had to be neglected. Finally, an isotropic temperature factor common to all crystallographic phases was used to compensate for residual mismatches in intensity.

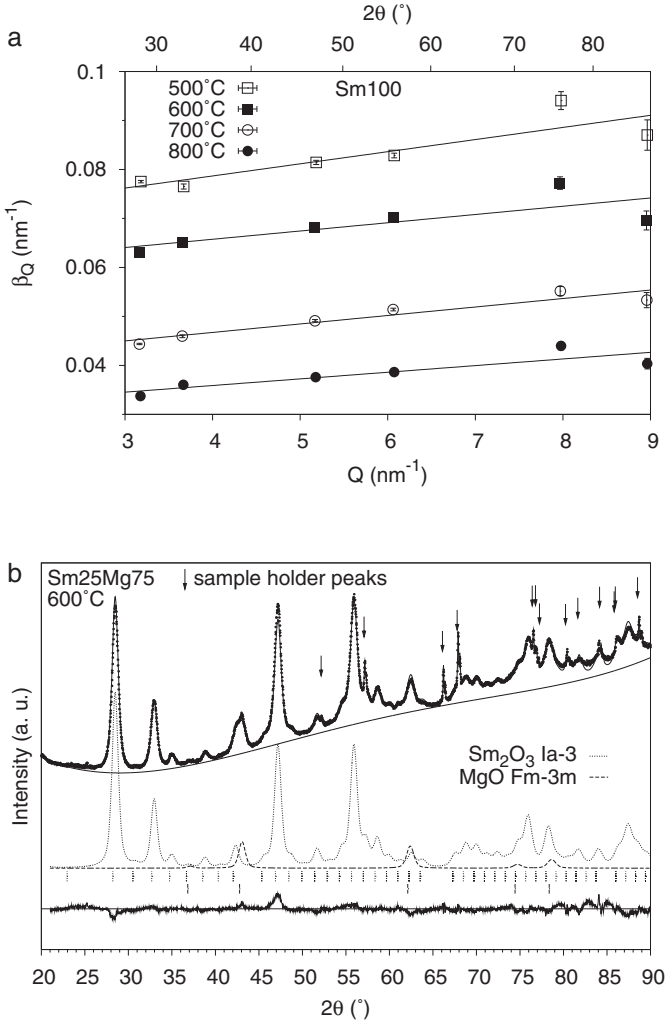

Fig. 3. (a) Williamson–Hall plots of sample Sm_{100} and (b) Rietveld refinement of sample $Sm_{25}Mg_{75}$. The samples were heat-treated in static air atmosphere for 12 h at the temperatures indicated.

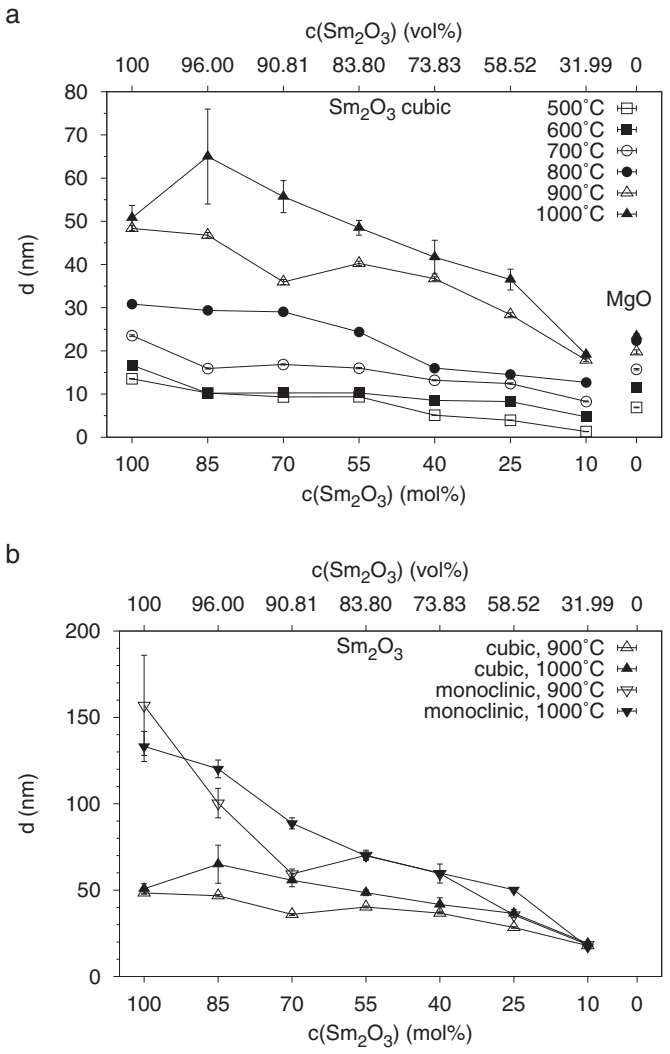

Fig. 4. Grain sizes of (a) cubic Sm_2O_3 and MgO and (b) cubic and monoclinic Sm_2O_3. The samples were heat-treated in static air atmosphere for 12 h at the temperatures indicated.

The Rietveld refinement of sample $Sm_{25}Mg_{75}$ heat-treated at 600 °C is depicted in Fig. 3b. The phase fractions of Sm_2O_3 and MgO are calculated to be 72.7 ± 0.7 wt% and 27.3 ± 0.7 wt%, respectively. This is in good agreement with the real values of 74.3 ± 0.3 wt% and 25.7 ± 0.3 wt% as determined by chemical analysis.[24] With decreasing amounts of MgO the determination of phase fractions is getting less accurate. While MgO in sample $Sm_{40}Mg_{60}$ can still be detected at all temperatures, heat treatments at 1000 °C are necessary in case of samples $Sm_{55}Mg_{45}$ and $Sm_{70}Mg_{30}$. The lowest phase fraction of MgO in sample $Sm_{85}Mg_{15}$ cannot be detected at all by XRD.

A very wide range of grain sizes is observed for cubic Sm_2O_3 depending on sample composition and temperature (Fig. 4a). The level of grain size naturally increases with temperature whereas the extent of grain growth is less the more MgO is present. The metastable to stable phase transformation from cubic to monoclinic Sm_2O_3 starts at around 800 °C and a big step in grain size is observed when 900 °C are reached. At 1000 °C the determination of grain size of cubic Sm_2O_3 is less accurate because the phase transformation is already well advanced. In addition, Fig. 4a also shows the grain sizes of MgO in sample Mg_{100}. At any temperature level the values are found to be much smaller than those of cubic Sm_2O_3 in sample Sm_{100}.

The influence of MgO on the grain growth of Sm_2O_3 is even more pronounced for the monoclinic phase. For comparison the grain sizes of both phases after heat treatments at 900 °C and 1000 °C are plotted in Fig. 4b. For sample $Sm_{10}Mg_{90}$ the grain sizes of cubic and monoclinic Sm_2O_3 are virtually the same independent of temperature. With decreasing amounts of MgO monoclinic grains show a stronger increase in size compared to cubic grains. When no MgO is present at all, monoclinic grains grow to up to three times the size of cubic grains.

3.3. Energy-filtered transmission electron microscopy

For the subsequent EFTEM analyses a reasonable selection had to be made from the 48 samples available after the HTXRD measurements. The samples $Sm_{70}Mg_{30}$, $Sm_{25}Mg_{75}$,

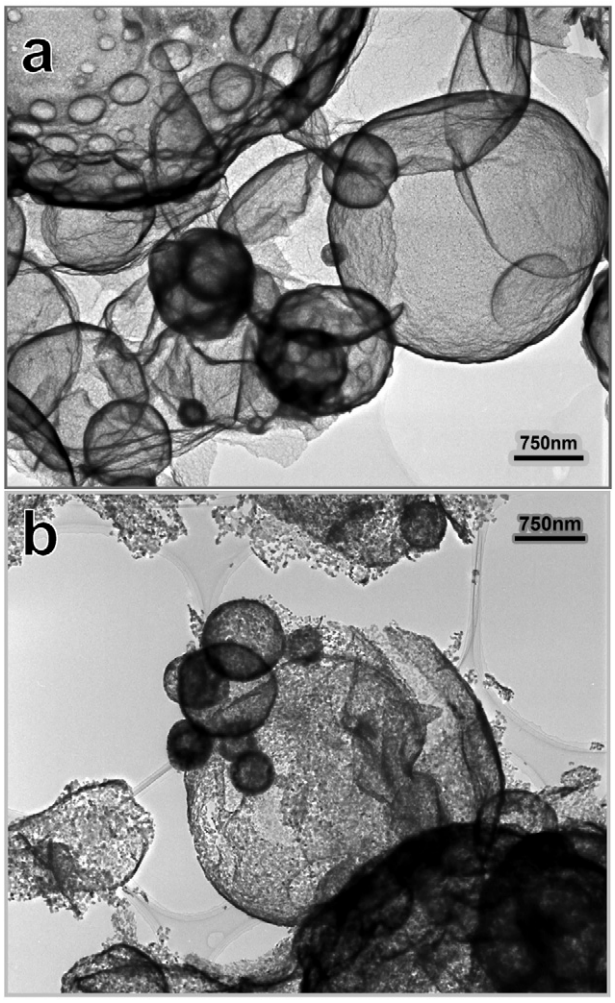

Fig. 5. Unfiltered TEM bright field images of sample $Sm_{25}Mg_{75}$ heat-treated in static air atmosphere for 12 h at (a) 500 °C and (b) 800 °C.

and $Sm_{10}Mg_{90}$ were chosen in order to cover a wide range of MgO volume fractions. Each of these samples were investigated after the HTXRD measurements at 500 °C and 800 °C. By this means the conditions immediately after complete crystallization and after extended grain growth but before the phase transformation of Sm_2O_3 could be analyzed.

A first visual impression is provided by Fig. 5a and b showing sample $Sm_{25}Mg_{75}$ after the low and high temperature treatment, respectively. At 500 °C many of the hollow spheres are still intact and no holes or pores are visible at the chosen magnification. However, at 800 °C significant changes of the morphology are observed. The shells are now composed of a granular network with a large number of holes. In consequence, the stability is reduced and the spheres start breaking apart.

Deeper insight into the microstructure is achieved by analyzing energy filtered images captured at high resolution. In Fig. 6a the bright field image of sample $Sm_{25}Mg_{75}$ heat-treated at 800 °C is displayed. Individual grains of different brightness are visible with distinct facettes, i.e. grain and phase boundaries with low curvature. In this arrangement the driving force for grain growth is already considerably reduced. The spatial

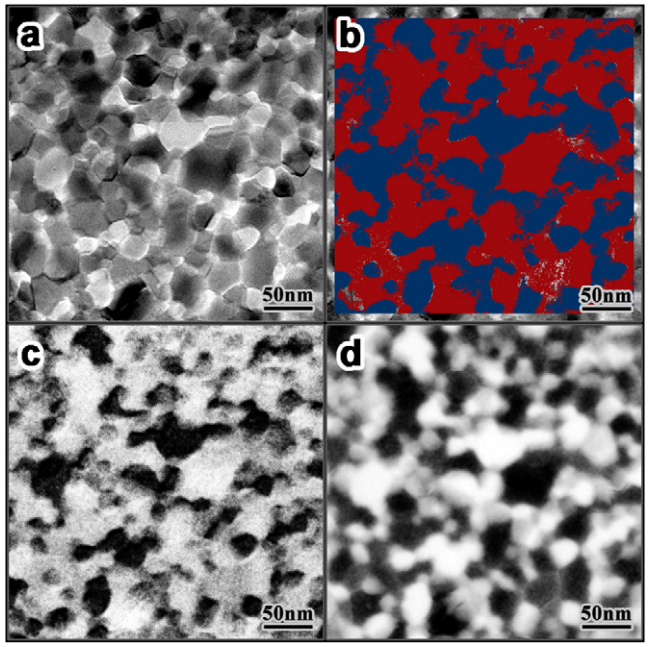

Fig. 6. EFTEM analysis of sample $Sm_{25}Mg_{75}$ heat-treated in static air atmosphere for 12 h at 800 °C: (a) bright field image, (b) overlay of the element distribution maps of samarium (red) and magnesium (blue), (c) element distribution map of samarium, (d) element distribution map of magnesium. (For interpretation of the references to color in this figure legend, the reader is referred to the web version of the article.)

distribution of samarium and magnesium is displayed in Fig. 6b. The false colors red and blue correspond to the bright areas of the element distribution maps shown in Fig. 6c and d, respectively. The element distribution maps correspond to each other like positive and negative images, i.e. by inverting the grayscales the samarium map almost perfectly resembles the magnesium map and vice versa. A comparison with the false color image clearly shows that in the bright field image dark areas originate from Sm_2O_3 grains while bright areas indicate MgO grains. This finding is in agreement with the difference in scattering absorption contrast which is higher for Sm_2O_3 than for MgO. However, the two metal oxides cannot unambigiously be distinguished since brightness depends on sample thickness and may also be affected by grains of different phases lying on top of each other.

Therefore, bright field images had to be binarized using an appropriate threshold. A reasonable approach is to adjust the black to white ratio according to the volume fractions of Sm_2O_3 and MgO (Fig. 7). By comparing the distribution and shape of black and white areas it becomes apparent that at 500 °C regardless of composition MgO exhibits a globular shape while Sm_2O_3 acts as the matrix phase (Fig. 7a, c, and e). This is ascribed to the lower thermal stability of the magnesium carboxylate complex compared to samarium leading to the primary precipitation of MgO.[24] The high dispersion of MgO points to a high nucleation rate provided by the homogeneous distribution of magnesium within the starting materials. At 800 °C the phase separation of Sm_2O_3 and MgO has further advanced (Fig. 7b, d, and f). With rising amounts of MgO a continuous transition takes place from mostly isolated MgO grains (Fig. 7b) via an intermediate

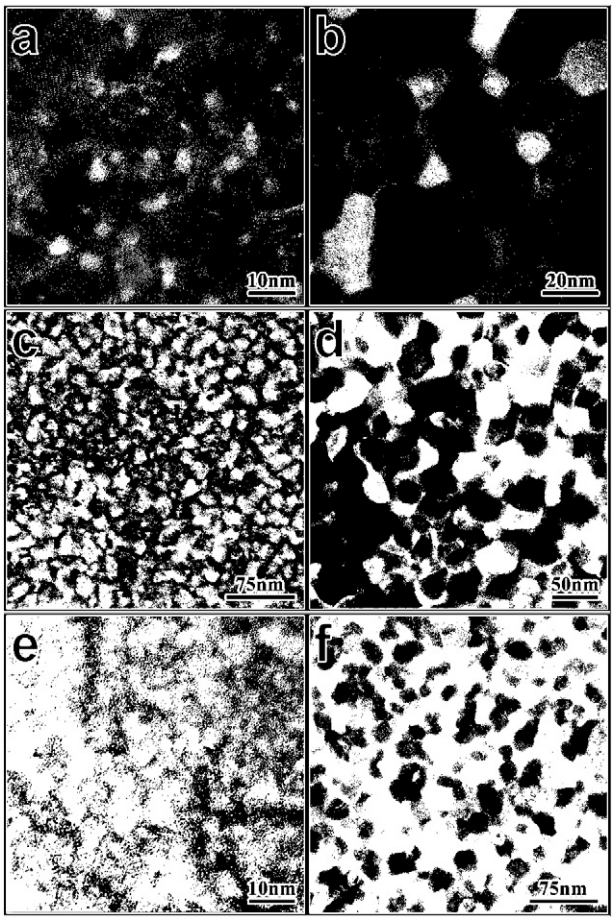

Fig. 7. EFTEM images of sample $Sm_{70}Mg_{30}$ (a, b), sample $Sm_{25}Mg_{75}$ (c, d), and sample $Sm_{10}Mg_{90}$ (e, f) heat-treated in static air atmosphere for 12 h at 500 °C (a, c, e) and 800 °C (b, d, f). The original grayscale images were binarized according to the volume fractions of Sm_2O_3 (black) and MgO (white).

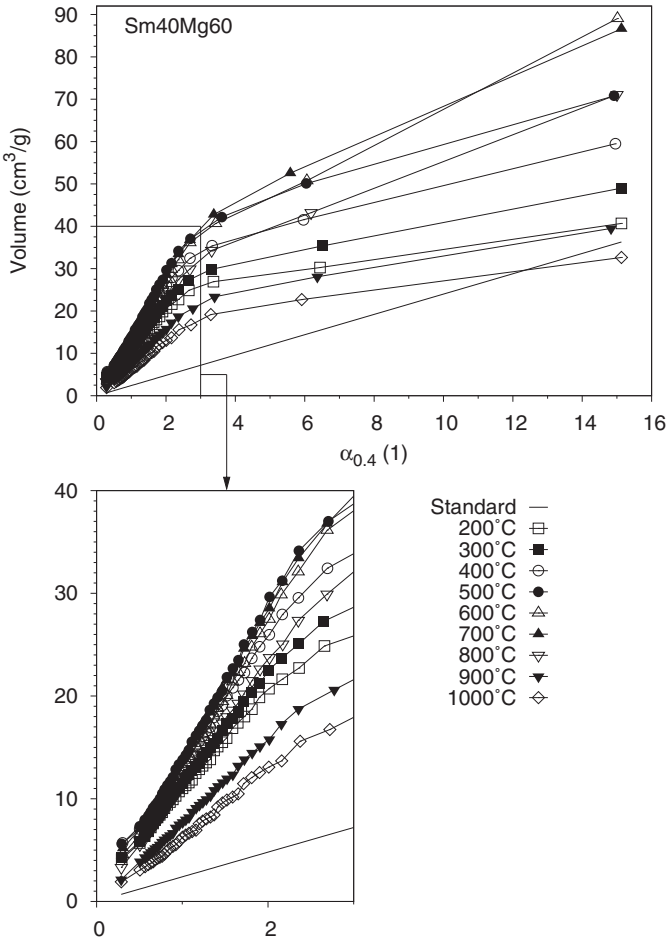

Fig. 8. $\alpha_{0.4}$-plots of sample $Sm_{40}Mg_{60}$ repeatedly heat-treated in static air atmosphere for 2 h at the temperatures indicated.

arrangement (Fig. 7d) to mostly isolated Sm_2O_3 grains (Fig. 7f).

3.4. Nitrogen adsorption

Using the example of sample $Sm_{40}Mg_{60}$ a full set of $\alpha_{0.4}$-plots is shown in Fig. 8. Although changes are noticed with each step in temperature, all curves exhibit two linear branches which are characteristic for the presence of microporosity. With the aid of the standard isotherm the specific surface area of micropores and the specific surface area of nonporous regions (hereinafter referred to as external surface area) can be calculated from the slopes of the first and second branch, respectively. The specific micropore volume is given by the *y*-axis intercept of the second branch. Since the sample densities depend on composition and temperature of the heat treatment a comparison of specific values based on sample mass is misleading. This difficulty was eliminated by repeatedly using the same batch of each sample for the complete temperature series. Thus, absolute values can be compared within the temperature series of a certain sample. In addition, comparability of samples with different compositions is achieved by normalization to the initial states, i.e. the corresponding values of the starting materials.[24]

The absolute surface area of micropores A_{int} divided by the absolute surface area of the starting materials A^0_{int} is depicted in Fig. 9a. A constant decline is observed for samples Sm_{100}, $Sm_{85}Mg_{15}$, $Sm_{70}Mg_{30}$, and $Sm_{55}Mg_{45}$. In contrast, the absolute surface areas of samples $Sm_{40}Mg_{60}$ and $Sm_{25}Mg_{75}$ slightly rise before they finally start to decline at temperatures above 400 °C. The increase is much higher for samples $Sm_{10}Mg_{90}$ and Mg_{100} with maximum values at 500 °C and 400 °C. However, bigger parts of the absolute surface areas are lost when temperatures approach 1000 °C. It is important to note that the ratio of surface area to volume of the micropores is constant for each sample composition throughout the entire temperature range. This suggests that the basic pore geometry remains unchanged during densification.

The evolution of the normalized absolute external surface area A_{ext}/A^0_{ext} is shown in Fig. 9b. Up to 500 °C an increase is noticed for all samples that is more pronounced the larger the amount of MgO. At 600 °C the external surface areas of samples with small amounts of MgO drop significantly while they are stable or even increase with samples comprising more than 45 mol% MgO. The further loss of A_{ext} at higher temperatures is less pronounced than for A_{int}.

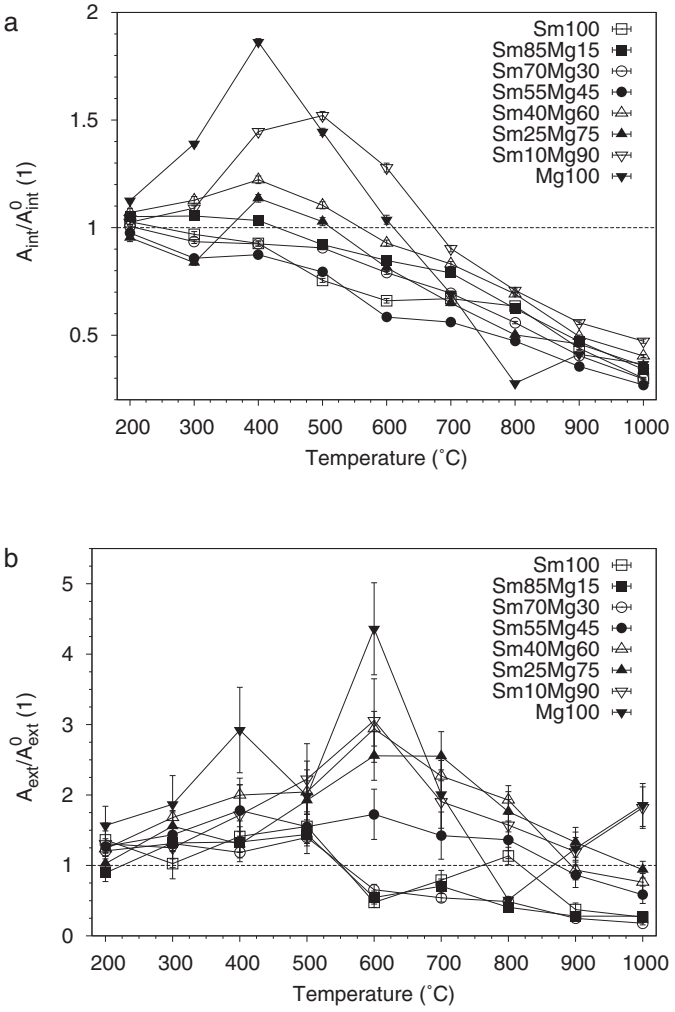

Fig. 9. Normalized absolute surface areas of (a) micropores and (b) nonporous regions. The samples were repeatedly heat-treated in static air atmosphere for 2 h at the temperatures indicated.

As soon as all samples have reached a fully crystalline state at around 500 °C reasonable assumptions can be made concerning the true densities. Based on the bulk densities of cubic Sm_2O_3 (7.31 g/cm^3) and MgO (3.576 g/cm^3) and with the knowledge of mass fractions the true density ρ of each sample can be calculated. The monoclinic phase of Sm_2O_3 can be neglected since the bulk density (7.68 g/cm^3) is just slightly higher and in addition only low fractions emerge below 800 °C. The micropore fraction of a sample with mass m is defined as the ratio of absolute micropore volume V_{int} to absolute envelope volume V_{env}:

$$\frac{V_{int}}{V_{env}} = \frac{V_{int}}{V_{int} + m/\rho} \tag{2}$$

The micropore fractions derived by Eq. (2) are plotted in Fig. 10. With rising temperature a decrease in micropore fractions is observed. The extent of densification is greater the higher the initial value of V_{int} which strongly depends on the amount of MgO. At 500 °C the micropore fraction increases evenly from pure Sm_2O_3 to sample $Sm_{25}Mg_{75}$. A sharp rise of V_{int} is observed when the amount of MgO is further increased

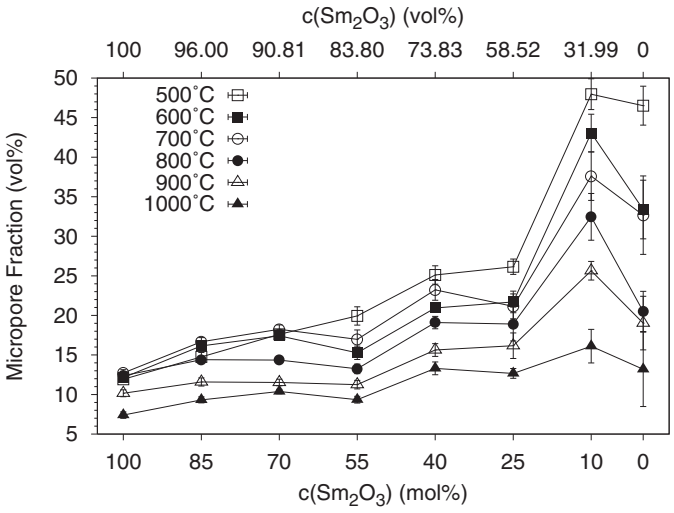

Fig. 10. Micropore fractions as derived by Eq. (2). The samples were repeatedly heat-treated in static air atmosphere for 2 h at the temperatures indicated.

to 90 mol%. Very similar characteristics are found at higher temperatures, only the influence of sample composition on the micropore fraction is continuously diminishing. It is interesting to note that at any temperature the maximum value is reached by sample $Sm_{10}Mg_{90}$.

3.5. Temperature programmed desorption of CO_2

In contrast to the physisorption of nitrogen, the chemisorption of CO_2 is specific to the surface chemical properties. Thus, the method of CO_2–TPD allows to distinguish Sm_2O_3 from MgO due to different basic surface sites. The CO_2–TPD curve of sample Sm_{100} is composed of three desorption signals (Fig. 11a). A small amount of weakly adsorbed CO_2 species emerges at 117 °C followed by the main fraction at 299 °C. Another small amount of stronger bound CO_2 desorbs not until 466 °C. The CO_2–TPD curve of sample Mg_{100} also reveals three desorption signals (Fig. 11b). Similar to sample Sm_{100}, the weakest and strongest desorption signals are found at 121 °C and 290 °C, respectively. However, in between a unique and quite strong desorption signal shows up at 197 °C.

An attempt was made to describe the CO_2–TPD curves of mixed samples using a simple rule of mixture. For that purpose the individual Gaussian functions used for the fits of sample Sm_{100} and sample Mg_{100} were summed up to yield the functions G^{tot}_{Sm} and G^{tot}_{Mg}. The CO_2–TPD curves of mixed samples should be reflected by the linear function $G^{tot}_{Sm/Mg}$:

$$G^{tot}_{Sm/Mg} = s\left(wG^{tot}_{Sm} + (1-w)G^{tot}_{Mg}\right) \tag{3}$$

From Eq. (3) the scaling factor s and the weighting factor w were used to fit the experimental data. In addition, offsets of G^{tot}_{Sm} and G^{tot}_{Mg} along the x-axis were handled by two parameters x_{Sm} and x_{Mg} and a single parameter y_0 was used to deal with different baseline offsets. It is noted that maximum offsets of approx. 100 s and 20 mV/g are observed. Reasonable fits are obtained for all of the mixed samples, one example is given

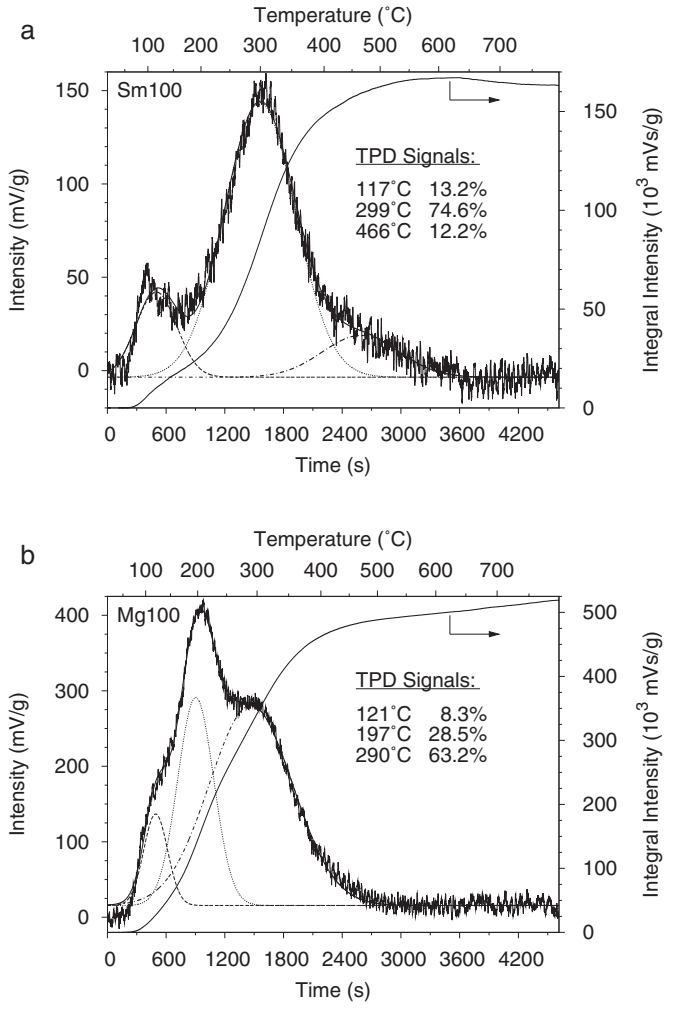

Fig. 11. CO_2–TPD curves of (a) sample Sm_{100} and (b) sample Mg_{100}. The samples were heat-treated in static air atmosphere for 12 h at 800 °C.

in Fig. 12. This proves that the nanocomposite formation does not affect the surface chemistry properties of Sm_2O_3 or MgO, i.e. the nature and distribution of basic surface sites remain the same.

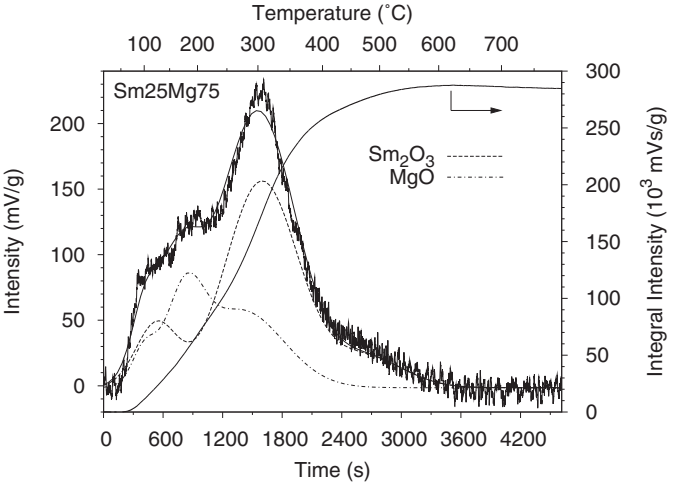

Fig. 12. CO_2–TPD curve of sample $Sm_{25}Mg_{75}$ heat-treated in static air atmosphere for 12 h at 800 °C.

A complete overview of the quantitative results from CO_2–TPD measurements is given in Table 1. All mixed samples exhibit higher mass-related specific CO_2 chemisorption capacities than sample Sm_{100} and even the value of sample Mg_{100} is at least exceeded by sample $Sm_{10}Mg_{90}$. If the chemisorption behaviors of Sm_2O_3 and MgO in mixed samples were identical to those of sample Sm_{100} and sample Mg_{100}, scaling factors of $s = 1$ and weighting factors equal to the amount of Sm_2O_3 in wt% would be observed. However, all parameters are to a greater or lesser extent higher than expected. The products sw and $s(1 - w)$ indicate how much of sample Sm_{100} and sample Mg_{100} would equal the specific CO_2 chemisorption capacities of the respective amounts of Sm_2O_3 and MgO in mixed samples. While all values of sw are much higher than $c(Sm_2O_3)$, most values of $s(1 - w)$ are only about equal to c(MgO) or even less. It is reasonable to assume that the specific CO_2 chemisorption capacities of Sm_2O_3 and MgO do not change with sample composition. Thus, the specific surface areas of Sm_2O_3 in mixed samples must be much higher than in sample Sm_{100} while the specific surface areas of MgO remain largely unchanged compared to sample Mg_{100}.

4. Discussion

Prior to discussing the underlying processes of thermal degradation the starting conditions have to be assessed, i.e. the sample properties immediately after the complete conversion of the starting materials into the inorganic nanocomposites. At 500 °C depending on the amount of MgO a very broad range of micropore fractions is observed (Fig. 10). The reason for this can be found in the evolution of microporosity during thermal decomposition of the starting material (Fig. 9a). While Sm-rich samples experience a constant loss of micropore surface area a significant gain is observed for Mg-rich samples. This may be attributed to differences in the steric configurations of samarium and magnesium carboxylate complexes which essentially predetermine type and amount of porosity after the burnout of organic components. Similarly, the larger the amount of MgO the stronger is the observed increase in external surface areas up to 600 °C (Fig. 9b).

In fact, the nanocomposites have to be considered as intimately mixed multi-phase materials consisting of various fractions of Sm_2O_3, MgO, and micropores. While the cubic phase of MgO is volume-conserved at any given temperature, Sm_2O_3 exhibits a metastable to stable phase transition starting from temperatures of about 800 °C. However, due to the small differences in density, the sum of both volumes is practically constant with temperature. In contrast, the micropore fraction is not volume-conserved at all, it continuously decreases at temperatures above 500 °C.

In general, the driving force for microstructural changes of metastable materials is provided by the excess energy ΔG. In case of porous multi-phase materials mainly surfaces (ΔG_{surf}), grain boundaries (ΔG_{gb}), and phase boundaries (ΔG_{pb}) contribute to the total value of ΔG:

$$\Delta G = \Delta G_{surf} + \Delta G_{gb} + \Delta G_{pb} \quad (4)$$

Table 1
Quantitative results of CO_2–TPD. The samples were heat-treated in static air atmosphere for 12 h at 800 °C. For explanation of parameters *s* and *w* see Eq. (3).

Sample	$c(Sm_2O_3)$ (wt%)	c(MgO) (wt%)	$n(CO_2)$ (μmol/g)	s (1)	w (1)	*sw* (%)	$s(1-w)$ (%)
Sm_{100}	100.00	–	68.6 ± 0.7	–	–	–	–
$Sm_{85}Mg_{15}$	98.0	2.0	91 ± 1	1.298 ± 0.003	0.985 ± 0.001	127.9 ± 0.4	1.9 ± 0.1
$Sm_{70}Mg_{30}$	95.3	4.7	100 ± 2	1.469 ± 0.004	1.000 − 0.001	146.9 ± 0.6	0.0 + 0.2
$Sm_{55}Mg_{45}$	91.4	8.6	76 ± 1	1.058 ± 0.003	0.966 ± 0.001	102.2 ± 0.4	3.6 ± 0.2
$Sm_{40}Mg_{60}$	85.2	14.8	119 ± 2	1.510 ± 0.003	0.894 ± 0.001	135.0 ± 0.5	16.0 ± 0.2
$Sm_{25}Mg_{75}$	74.3	25.8	111 ± 2	1.291 ± 0.003	0.827 ± 0.001	106.8 ± 0.4	22.3 ± 0.2
$Sm_{10}Mg_{90}$	49.0	51.0	191 ± 3	2.050 ± 0.005	0.757 ± 0.002	155.1 ± 0.7	49.9 ± 0.4
Mg_{100}	–	100	170 ± 2	–	–	–	–

For microporous Sm_2O_3–MgO nanocomposites the individual excess energies can further be broken down as follows:

$$\Delta G_{surf} = \gamma_{Sm-p}\Delta A_{Sm-p} + \gamma_{Mg-p}\Delta A_{Mg-p} \quad (5)$$

$$\Delta G_{gb} = \gamma_{Sm-Sm}\Delta A_{Sm-Sm} + \gamma_{Mg-Mg}\Delta A_{Mg-Mg} \quad (6)$$

$$\Delta G_{pb} = \gamma_{Sm-Mg}\Delta A_{Sm-Mg} \quad (7)$$

In Eqs. (5)–(7) γ and ΔA denote the specific energies and areas of particular interfaces. Surfaces exist at the interfaces between either Sm_2O_3 (Sm) or MgO (Mg) and pores (p). Grain boundaries are the interfaces between either grains of Sm_2O_3 or MgO and phase boundaries are formed when Sm_2O_3 is in contact with MgO. Phase boundaries between cubic and monoclinic Sm_2O_3 are neglected here since they only evolve at higher temperatures. In principle, a change in microstructure can only occur in the direction of the thermodynamic gradient towards the minimum of the Gibbs energy ($\Delta G \rightarrow 0$). If all interfacial energies are assumed to be constant this can only be achieved by reducing the interfacial areas.

In a theoretic work Gouvêa and Castro[30] demonstrated that densification and grain growth behavior of ceramic materials depend on the ratio of interfacial energies. This is because in contrast to most sinter metals the grain boundary energies are not negligibly small compared to surface energies. A densification factor K was defined which is related to the dihedral angle $\theta = \arccos\left(\gamma_{gb}/2\gamma_p\right)$ where γ_{gb} and γ_p are the grain boundary and pore surface energy, respectively. Densification is dominating for $\gamma_{gb} \ll \gamma_p$ ($K \rightarrow \infty$, $\theta \rightarrow 90°$) while mainly grain growth occurs for $\gamma_{gb} \rightarrow 2\gamma_p$ ($K \rightarrow 0$, $\theta \rightarrow 0°$). For MgO a ratio of $\gamma_{gb}/\gamma_p = 1.1$ was determined from calorimetric measurements[31], i.e. there is some intrinsic resistance against densification. Unfortunately, no such data is available for Sm_2O_3.

Many works can be found in literature dealing with the microstructural evolution and grain growth kinetics of fully dense two-phase composites. In most cases different types of two-dimensional Monte Carlo simulation techniques were applied to systemically assess the impact of interfacial energies and volume fractions of the two phases in systems with both non-conserved[32] and conserved phase volumes.[33–36] The element distribution maps of sample $Sm_{25}Mg_{75}$ with a Sm_2O_3 to MgO volume ratio of 59:41 show clusters of approximately equiaxed grains of same phases (Fig. 6b). Phase separation caused ΔA_{Sm-Mg} to decrease and necessarily ΔA_{Sm-Sm} and ΔA_{Mg-Mg} to increase. This is only possible when γ_{Sm-Mg} (Eq. (7)) is higher than both γ_{Sm-Sm} and γ_{Mg-Mg} (Equation 6). Otherwise the system would avoid clustering and favor elongated grains in order to reduce ΔA_{Sm-Sm} and ΔA_{Mg-Mg} [33]. This finding is supported by the microstructure of sample $Sm_{70}Mg_{30}$ shown in Fig. 7b. Here MgO is the minor phase and grain boundary wetting would be observed if $\gamma_{Sm-Sm} > 2\gamma_{Sm-Mg}$.[35] In summary, the following thermodynamic relations could be derived: $\gamma_{Sm-Mg} > \gamma_{Sm-Sm}$ and $\gamma_{Sm-Mg} > \gamma_{Mg-Mg} > \gamma_{Mg-p}$. Unfortunately, it is not possible to assess the relations between γ_{Sm-p} and γ_{Mg-p} and between γ_{Sm-Sm} and γ_{Mg-Mg}.

The situation is further complicated because the initial micropore fractions strongly correlate with the amount of MgO. In order to retrace the major aspects of thermal degradation it is instructive to focus on two samples comprising very different amounts of MgO:

The actual composition of sample $Sm_{70}Mg_{30}$ at 500 °C is approx. 75 vol% Sm_2O_3, 7 vol% MgO, and 18 vol% micropores. If the probability for the occurrence of a specific type of interface is assumed to scale with the volume fractions of the phases involved, ΔA_{Sm-Sm} is by far the most frequent one followed by ΔA_{Sm-p}, ΔA_{Sm-Mg}, ΔA_{Mg-p}, and ΔA_{Mg-Mg}. Thus, reducing the grain boundary area of Sm_2O_3 has the highest potential to reduce ΔG. Grain boundary movement cannot be the predominant growth mechanism because the Sm_2O_3 grain boundary network is severely disturbed by the presence of finely dispersed MgO and microporosity. Instead, the increase in grain size must rather be the result of coarsening processes. In general, the mass flux per unit volume is inversely proportional to the characteristic diffusion distance. This distance is increased by the presence of MgO because the average coordination number of Sm_2O_3 grains is reduced [37] and thus some grain growth inhibition is observed (Fig. 4a). Micropores have a similar effect, but only as long as they can resist densification. Phase separation (reduction of ΔA_{Sm-Mg}) and coarsening of MgO grains (reduction of ΔA_{Mg-Mg}) are impeded by the high spatial separation (Fig. 7a and b) and thus the prerequisite for second phase stabilization are met even at higher temperatures. However, particular strong grain growth of Sm_2O_3 is noticed during the reconstructive phase transformation because newly formed monoclinic grains can easily grow across the grain boundaries of adjacent cubic grains (Fig. 4b). Below 800 °C hardly any densification (reduction of ΔA_{Sm-p} and ΔA_{Mg-p}) is observed. Densification is generally associated with either grain boundary or lattice diffusion from grain boundaries to sintering necks.[38] Again, the

mass flux per unit volume is inversely proportional to the characteristic diffusion distance which was found to scale with the distance between nearest neighboring pores.[39] Thus, the lower the micropore fraction the higher temperatures are necessary to achieve densification (Fig. 10).

The situation is very different for sample $Sm_{10}Mg_{90}$ at 500 °C with an actual composition of only 17 vol% Sm_2O_3 but 35 vol% MgO and 48 vol% micropores. Here, ΔA_{Mg-p} is the most frequent type of interface followed by ΔA_{Mg-Mg}, ΔA_{Sm-p}, ΔA_{Sm-Mg}, and ΔA_{Sm-Sm}. Due to the low solid volume fraction the average micropore distance is small and consequently very strong densification is observed (Fig. 10). Nevertheless, compared to sample Mg_{100} densification is slightly less severe. There is a sizeable probability that ΔA_{Mg-p} and ΔA_{Sm-p} can only be replaced by ΔA_{Sm-Mg} but not by ΔA_{Mg-Mg} and ΔA_{Sm-Sm}, respectively. This is thermodynamically less favorable and thus densification is potentially retarded. With 35 vol% the stabilizing effect of MgO on Sm_2O_3 is not the reduction of average coordination number anymore but the formation of a second phase rigid network [37] (Fig. 7a). In addition, the micropore fraction is high at any temperature and thus coarsening of Sm_2O_3 grains is drastically reduced (Fig. 4a). The grain size remains virtually unchanged during the phase transformation because most of the Sm_2O_3 grains are separated from each other by either MgO grains or micropores (Fig. 4b).

Finally, the CO_2–TPD measurements revealed that Sm_2O_3 disproportionately contributes to the total specific surface area, especially in case of sample $Sm_{10}Mg_{90}$ (Table 1). Since the total specific surface area is increased while the grain size is decreased, it is not surprising that the degree of dispersion of Sm_2O_3 in mixed samples is significantly higher compared to sample Sm_{100}.

5. Conclusions

The in-depth analysis of microporous Sm_2O_3–MgO nanocomposites revealed the major mechanisms of thermal degradation caused by heat treatments at different temperatures in the range of 500–1000 °C. The characteristic diffusion distances were found to be of decisive importance for the extent of grain growth and densification. They are directly related to the phase fractions of Sm_2O_3, MgO, and micropores which are determined by the ratio of samarium to magnesium in the starting materials.

Small additions of MgO only lead to little increase in microporosity compared to pure Sm_2O_3. Here, the main impact of thermal degradation is coarsening of Sm_2O_3 grains. The grain growth inhibiting effect of both MgO and micropores is based on the increase of the characteristic diffusion distance through the reduction of average coordination number. Densification is rather weak because the small number of micropores are well separated by the solid phases.

In contrast, with large amounts of MgO a very strong increase in microporosity is observed. Furthermore, when the percolation threshold is reached MgO forms a second phase rigid network. Under these conditions, coarsening of Sm_2O_3 only plays a minor role because most diffusion paths are virtually blocked. However, densification can hardly be avoided because low solid phase fractions entail short characteristic diffusion distances between nearest neighboring pores.

The Sm_2O_3–MgO nanocomposites do not show any change of surface chemistry properties with respect to pure Sm_2O_3 and MgO. However, the specific CO_2 chemisorption capacities are higher because the specific surface area of Sm_2O_3 is increased through the addition of MgO. Thus, the nanocomposite formation allows for a more efficient and economic utilization of the rather costly rare earth oxide.

References

1. Hahn H. Unique features and properties of nanostructured materials. *Adv Eng Mater* 2003;**5**(5):277–84.
2. Raimondi F, Scherer GG, Kotz R, Wokaun A. Nanoparticles in energy technology: examples from electrochemistry and catalysis. *Angew Chem Int Ed* 2005;**44**(15):2190–209.
3. Goesmann H, Feldmann C. Nanoparticulate functional materials. *Angew Chem Int Ed* 2010;**49**(8):1362–95.
4. Raveendran Shiju N, Guliants VV. Recent developments in catalysis using nanostructured materials. *Appl Cat A-Gen* 2009;**356**(1):1–17.
5. Tanabe K, Hölderlich WF. Industrial application of solid acid–base catalysts. *Appl Cat A-Gen* 1999;**181**(2):399–434.
6. Hattori H. Solid base catalysts: generation, characterization, and catalytic behavior of basic sites. *J Jpn Petrol Inst* 2004;**47**(2):67–81.
7. Maitra AM. Critical performance evaluation of catalysts and mechanistic implications for oxidative coupling of methane. *Appl Cat A-Gen* 1993;**104**(1):11–59.
8. Bartholomew CH. Mechanisms of catalyst deactivation. *Appl Catal A-Gen* 2001;**212**(1-2):17–60.
9. Ying JY, Sun T. Research needs assessment on nanostructured catalysts. *J Electroceram* 1997;**1**(3):219–38.
10. Tanabe K, Misono M, Ono Y, Hattori H. Acid and base centers: structure and acid–base property. In: *Studies in surface science and catalysis 51: new solid acids and bases: their catalytic properties.* Amsterdam: Elsevier; 1989. p. 27–213.
11. Keller GE, Bhasin MM. Synthesis of ethylene via oxidative coupling of methane: I. Determination of Active Catalysts. *J Catal* 1982;**73**(1):9–19.
12. Amenomiya Y, Birss VI, Goledzinowski M, Galuszka J, Sanger AR. Conversion of methane by oxidative coupling. *Catal Rev* 1990;**32**(3):163–227.
13. Wendt G, Schaffarczyk S. Oxidative Dimerisierung von Methan an Mischoxidkatalysatoren. *Chem Technol* 1991;**43**(4):131–40.
14. Lunsford JH. Recent advances in the oxidative coupling of methane. In: Curry-Hyde HE, Howe RF, editors. *Studies in surface science and catalysis 81: natural gas conversion II: proceedings of the third natural gas conversion symposium*. Amsterdam: Elsevier; 1994. p. 1–12.
15. Lunsford JH. The catalytic oxidative coupling of methane. *Angew Chem Int Ed* 1995;**34**(9):970–80.
16. Otsuka K, Jinno K, Morikawa A. The catalysts active and selective in oxidative coupling of methane. *Chem Lett* 1985;**14**(4):499–500.
17. Ito T, Tashiro T, Watanabe T, Toi K, Ikemoto I. Activation of methane on the MgO surface at low temperatures. *Chem Lett* 1987;**16**(9): 1723–6.
18. Ito T, Lunsford JH. Synthesis of ethylene and ethane by partial oxidation of methane over lithium-doped magnesium oxide. *Nature* 1985;**314**(6013):721–2.
19. Ito T, Wang JX, Lin CH, Lunsford JH. Oxidative dimerization of methane over a lithium-promoted magnesium oxide catalyst. *J Am Chem Soc* 1985;**107**(18):5062–8.
20. Shestov AA, Muzykantov VS, Tyulenin YP, Kadushin AA. Exchange isotope kinetics and activation mechanisms of methane and oxygen on the oxide catalysts of oxidative coupling of methane—Sm_2O_3/MgO and Nd_2O_3/MgO. *Catal Today* 1992;**13**(4):579–80.

21. Buyevskaya OV, Rothaemel M, Zanthoff HW, Baerns M. Transient studies on the role of oxygen activation in the oxidative coupling of methane over Sm_2O_3, Sm_2O_3/MgO, and MgO catalytic surfaces. *J Catal* 1994;**150**(1):71–80.
22. Ciambelli P, Lisi L, Pirone R, Ruoppolo G, Russo G. Comparison of behaviour of rare earth containing catalysts in the oxidative dehydrogenation of ethane. *Catal Today* 2000;**61**(1-4):317–23.
23. Choudhary VR, Rane VH. Oxidative coupling of methane over Sm-promoted MgO: influence of composition and preparation conditions. *J Chem Technol Biotechnol* 1997;**70**(4):325–30.
24. Enz T, Sieger H, Fasel C, Hahn H. Nanocomposite formation through thermal decomposition of mixed samarium and magnesium citrate-derived gels formed by spray pyrolysis. *J Am Ceram Soc* 2008;**91**(9): 3066–73.
25. Young RA, Wiles DB. Profile shape functions in Rietveld refinements. *J Appl Crystallogr* 1982;**15**(4):430–8.
26. Cheary RW, Coelho A. A fundamental parameters approach to X-ray line-profile fitting. *J Appl Crystallogr* 1992;**25**(2):109–21.
27. Williamson GK, Hall WH. X-ray line broadening from filed aluminium and wolfram. *Acta Metall Mater* 1953;**1**(1):22–31.
28. Stokes AR, Wilson AJC. The diffraction of X-rays by distorted crystal aggregates—I. *P Phys Soc* 1944;**56**(3):174–81.
29. Balzar D. Voigt function model in diffraction-line broadening analysis. In: Snyder RL, Fiala J, Bunge HJ, editors. *IUCr monographs on crystallography 10: defect and microstructure analysis by diffraction*. New York: Oxford University Press; 1999. p. 94–126.
30. Gouvêa D, Castro RHR. Sintering The role of interface energies. *Appl Surf Sci* 2003;**217**(1–4):194–201.
31. Castro RHR, Tôrres RB, Pereira GJ, Gouvêa D. Interface energy measurement of MgO and ZnO: understanding the thermodynamic stability of nanoparticles. *Chem Mater* 2010;**22**(8):2502–9.
32. Holm EA, Srolovitz DJ, Cahn JW. Microstructural evolution in two-dimensional two-phase polycrystals. *Acta Metall Mater* 1993;**41**(4): 1119–36.
33. Fan D, Chen LQ. Diffusion-controlled grain growth in two-phase solids. *Acta Metall Mater* 1997;**45**(8):3297–310.
34. Fan D, Chen LQ. Computer simulation of grain growth and Ostwald ripening in alumina–zirconia two-phase composites. *J Am Ceram Soc* 1997;**80**(7):1773–80.
35. Ohnuma I, Ishida K, Nishizawa T. Computer simulation of grain growth in dual-phase structures. *Philos Mag A* 1999;**79**(5):131–44.
36. Zheng YG, Lu C, Mai YW, Gu YX, Zhang HW, Chen Z. Monte Carlo simulation of grain growth in two-phase nanocrystalline materials. *Appl Phys Lett* 2006;**88**(14):144103.
37. Kumar KNP. Porous nanocomposites as catalyst supports: part I. 'Second phase stabilization', thermal stability and anatase-to-rutile transformation in titania-alumina nanocomposites. *Appl Catal A-Gen* 1994;**119**(1):163–83.
38. Ashby MF. A first report on sintering diagrams. *Acta Metall Mater* 1974;**22**(3):275–89.
39. Chen T, Nettleship I, McAfee RJ. An experimental measurement of effective diffusion distance for the sintering of ceramics. *J Am Ceram Soc* 2009;**92**(7):1481–6.